J. Astrophys. Astr. (2023) 44:34
https://doi.org/10.1007/s12036-023-09930-2

STAR FORMATION

Investigating morphology and CO gas kinematics of Sh2-112 region

KSHITIZ K. MALLICK[1,*], SAURABH SHARMA[1], LOKESH K. DEWANGAN[2], DEVENDRA K. OJHA[3], NEELAM PANWAR[1] and TAPAS BAUG[4]

[1]Aryabhatta Research Institute of Observational Sciences (ARIES), Manora Peak, Nainital 263002, India.
[2]Physical Research Laboratory, Navrangpura, Ahmedabad 380009, India.
[3]Department of Astronomy and Astrophysics, Tata Institute of Fundamental Research, Homi Bhabha Road, Mumbai 400005, India.
[4]S.N. Bose National Centre for Basic Sciences, Block JD, Sector III, Salt Lake, Kolkata 700106, India.
*Corresponding author. E-mail: kshitiz@aries.res.in

MS received 8 November 2022; accepted 4 January 2023

Abstract. We present a study of the molecular cloud in Sh2-112 massive star forming region using the 3-2 transition of CO isotopologues: CO, ^{13}CO and C^{18}O; supplemented in part by CGPS H I line emission and MSX data. Sh2-112 is an optically visible region powered by an O8V type massive star BD+45 3216, and hosts two Red MSX Survey sources: G083.7962+03.3058 and G083.7071+03.2817, classified as H II region and young stellar object, respectively. Reduced spectral data products from the James Clerk Maxwell Telescope archive, centered on the two RMS objects with $\sim 7' \times 7'$ field-of-view each, were utilized for the purpose. The ^{13}CO(3-2) channel map of the region shows the molecular cloud to have filamentary extensions directed away from the massive star, which also seems to be at the edge of a cavity like structure. Multiple molecular cloud protrusions into this cavity structure, host local peaks of emission. The integrated emission map of the region constructed from only those emission clumps, detected above 5σ level in the position–position–velocity space affirms the same. MSX sources were found distributed along the cavity boundary, where the gas has been compressed. Spectral extraction at these positions yielded high Mach numbers and low ratios of thermal to non-thermal pressures, suggesting a dominance of supersonic and non-thermal motion in the cloud.

Keywords. Interstellar filaments—H II regions—millimeter astronomy—star formation—massive stars.

1. Introduction

Formation and evolution of massive stars is a significant area of research (Zinnecker & Yorke 2007), as such stars can affect the evolution of the Galaxy via their immense matter and radiation output. Though it has been difficult to establish an evolutionary sequence for massive stars, due to their faster evolution and relatively rarer occurrences, various high-mass precursors have been sought to be established, such as massive cold molecular cores, massive starless clumps, infrared dark clouds (IRDCs) (Motte *et al.* 2018), massive young stellar objects (MYSOs) (Hoare *et al.* 2005), and so on. The Lyman continuum radiation from high-mass stars ionizes the surrounding medium, and the subsequent expanding H II regions have been the subjects of investigation for understanding the impact of radiation output in triggering or quenching further star formation in the natal cloud (Elmegreen 1998, 2011; Ogura 2010).

Sh2-112 is an optically visible H II region (Dickel *et al.* 1969) (Figure 1) ($l \sim 83.758°$, $b \sim +03.275°$) at a distance of 2 kpc (Panwar *et al.* 2020) in the northern Galactic plane. It is associated with the Cygnus superbubble, and is one of the many Sharpless (Sharpless 1959) H II regions in Cygnus (Uyanıker *et al.* 2001). The region appears nearly circular at optical wavelengths, and displays a blister morphology in radio emission (Israel 1978). Figure 1 displays a prominent dark lane against the optical emission. The massive star BD+45 3216—which has been estimated to be of spectral type

This article is part of the Special Issue on "Star formation studies in the context of NIR instruments on 3.6m DOT".

Published online: 15 April 2023

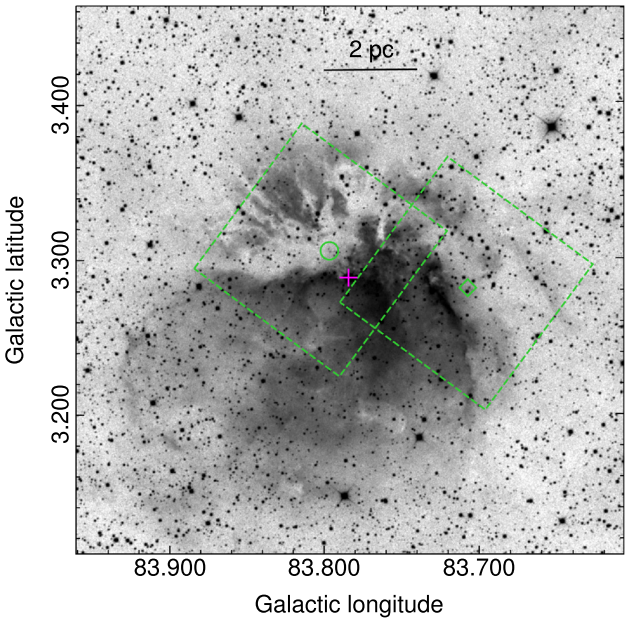

Figure 1. DSS2-red image of the Sh2-112 region. Plus symbol marks the massive star BD+45 3216. Circle and diamond denote the locations of the two RMS sources, G083.7962+03.3058 and G083.7071+03.2817, respectively. Dashed boxes show the field-of-view of the two JCMT fields.

O8V (Lahulla 1985; Panwar *et al.* 2020)—lies close to this lane, off-center from the optical nebulosity. The Red MSX Source (RMS) survey by Lumsden *et al.* (2013)—which aims to catalog massive young stellar population in the Galaxy—has identified two sources associated with the Sh2-112 region, namely, G083.7962+03.3058 and G083.7071+03.2817, classified as H II region and YSO, respectively, in the catalog. Though the molecular cloud in this region has been subjected to investigations in literature in various molecular transitions, such as HCN ($J = 1$–0) (Burov *et al.* 1988), CO (Blitz *et al.* 1982), ^{13}CO ($J = 1$–0) (Dobashi *et al.* 1994, 1996) and CO isotopologues (Urquhart *et al.* 2008; Maud *et al.* 2015b; Panja *et al.* 2022), they have either been at a low resolution, and/or as a part of a large statistical study or a larger region encompassing Sh2-112. As such, a detailed examination of the molecular cloud associated with Sh2-112 H II region is pending, a void we try to fill in this paper.

The organization of this paper is as follows. In Section 2, we list the datasets used and any processing steps taken. This is followed by Section 3, where we present the analysis results for the molecular gas kinematics. Finally, we discuss our results in Section 4, followed by a summary and conclusions in Section 5.

2. Data used

2.1 *Archival spectral data products*

We obtained the archival reduced and calibrated James Clerk Maxwell Telescope (JCMT) spectral cubes from the Canadian Astronomy Data Centre[1] (CADC), for CO(3-2) (rest frequency = 345.79599 GHz), ^{13}CO (3-2) (rest frequency = 330.587960 GHz), and C^{18}O (3-2) (rest frequency = 329.330545 GHz). The $J = 3$–2 transition traces gas at a critical density of $\sim 10^{4-5}$ cm^{-3} (Buckle *et al.* 2010). In the direction of the Sh2-112 region, two fields have been observed by the JCMT, namely, G083.7962+03.3058 and G083.7071+03.2817 (see Figure 1), using the Heterodyne Array Receiver Programme/Auto-Correlation Spectral Imaging System (HARP/ACSIS; Buckle *et al.* 2009). Cubes for both of these fields were retrieved. The temperature scale used for the pixel brightness units is T_A^* (antenna temperature). A basic processing using the STARLINK KAPPA (Currie *et al.* 2014) package was carried out, wherein the downloaded reduced cubes for the two fields were mosaiced; the spectral axis was converted to LSRK velocity scale; and the coordinate system was transformed to Galactic from FK5 for ease of analysis. Thereafter, the cubes were rebinned along spectral axis to 0.5 km s^{-1} channel width. Table 1 provides the details of the JCMT data used. While the rebinned cubes were used for the detection of spatial structures (Sections 3.1 and 3.2), as they have lower RMS noise; for the calculation of physical parameters (Section 3.3) the native channel width (^{13}CO and/or C^{18}O) cubes were used as high velocity resolution is required for the same.

For the Sh2-112 region, we also procured archival spectral cube for 21 cm H I line emission produced by the Canadian Galactic Plane Survey (CGPS) Consortium (Taylor *et al.* 2003). We use the cube on an as is basis for examining the morphology of the region. The 21 cm cube has an angular resolution of $\sim 1' \times 1'$ cosec δ, channel width of $\sim$0.8 km s^{-1} and a velocity resolution of $\sim$1.3 km s^{-1}.

2.2 *Archival imaging data products*

We obtained the stellar sources present in Midcourse Space Experiment (MSX) Catalog 6 (Egan *et al.* 2003) for our JCMT field-of-view, via the NASA/IPAC Infrared Science Archive.[2] Though observations by the MSX satellite were carried out in six bands ranging from

[1] https://www.cadc-ccda.hia-iha.nrc-cnrc.gc.ca/en/.
[2] https://irsa.ipac.caltech.edu/.

Table 1. JCMT data used.

Line/ Wavelength	Spatial resolution	Native channel width (km s^{-1})	Rebinned channel width (and noise)	Program IDs used
CO(3-2)	∼14″	∼0.42	0.5 km s^{-1} (∼0.37 K)	M08AU19
^{13}CO(3-2)	∼14″	∼0.05	0.5 km s^{-1} (∼0.35 K)	M08AU19, M08BU18
$C^{18}O$(3-2)	∼14″	∼0.05	0.5 km s^{-1} (∼0.45 K)	M08AU19, M08BU18

4 to 21 μm, the most sensitive observation has been in the mid-infrared (MIR) A band (8.28 μm; Lumsden *et al.* 2002). The other three MIR bands used by MSX are C (12.13 μm), D (14.65 μm) and E (21.3 μm). MSX has surveyed the Galactic plane at MIR bands with a spatial resolution of ∼18.3″ (Price *et al.* 2001), and has helped in uncovering its MIR population, especially the deeply embedded stellar objects (Lumsden *et al.* 2002).

Besides the above, Hα image from the IPHAS[3] (Drew *et al.* 2005; Barentsen *et al.* 2014) survey (Obs date: 14-08-2003); the DSS2-red image;[4] and the NRAO VLA Sky Survey (NVSS; Condon *et al.* 1998) 1.4 GHz continuum image was downloaded for a visual examination of the region.

3. Results

3.1 *Channel maps*

Figure 2 shows the channel map for the Sh2-112 region in ^{13}CO(3-2) emission. The massive star BD+45 3216 and the two RMS sources (G083.7962+03.3058 and G083.7071+03.2817) have been marked on the image. The filamentary nature of the molecular emission is clearly brought out in the channel maps. While in the eastern part, different filamentary structures seem to join at one end at the RMS source G083.7962+03.3058 (circle); in the western portion, such structures seem to converge on G083.7071+03.2817 (diamond symbol). In the velocity range of −4.0 to −2.0 km s^{-1}, the two parts seem to be connected by molecular filaments. Another noticeable feature is that in the eastern part, the molecular emission forms an arc-like structure directed away from the massive star BD+45 3216 (plus symbol), best delineated in the [−2.0, −1.0] km s^{-1} panel. While in the velocity range of [−2.0, 0.0] km s^{-1}, this arc appears to be directed towards north; at the blueshifted velocities, for example, [−7.0, −5.0] km s^{-1} range, it appears curved towards the south. In the middle velocity ranges, [−5.0, −2.0] km s^{-1}, no proper pattern can be made out. It is possible that two separate filaments, seen at blueshifted and redshifted velocities, respectively, are merging at this juncture. Towards the north-west of the massive star BD+45 3216, there appears to be a cavity, where hardly any molecular emission is seen. Furthermore, the western emission centered on the G083.7071+03.2817 source is also directed away from the massive star.

3.2 *Moment maps*

In this section, we examine the m-0 (moment-0 or integrated intensity), m-1 (moment-1 or intensity-weighed velocity), and linewidth (intensity-weighed dispersion) maps of the molecular emission in the Sh2-112 region. The examination is confined to only those regions, which are detected at ≥5σ detection level in the spectral cubes (σ being the rms noise level of the respective cubes). To achieve this, the clumpfind algorithm of Williams *et al.* (1994) was utilized via STARLINK software's (Currie *et al.* 2014) CUPID package (Berry *et al.* 2007). The 5σ threshold was conservatively chosen to eliminate false detections of clumps. As recommended by Williams *et al.* (1994), the gap between contour levels was kept at 2σ. With these values, the clumpfind algorithm was implemented on the mosaiced CO(3-2), ^{13}CO(3-2) and $C^{18}O$(3-2) position–position–velocity cubes. After the detection of clumps, we mask those regions where no emission was detected at 5σ or above to create a masked cube. Thereafter, the respective (masked) cubes were collapsed to create m-0, m-1 and linewidth images.

The maps are shown in Figure 3 for CO(3-2), ^{13}CO(3-2) and $C^{18}O$(3-2) molecular transitions. The massive star BD+45 3216 and the two RMS sources (G083.7962+03.3058 and G083.7071+03.2817) have been marked on each of the images. In the m-0 maps,

[3] https://www.iphas.org/images/.

[4] https://archive.eso.org/dss/dss.

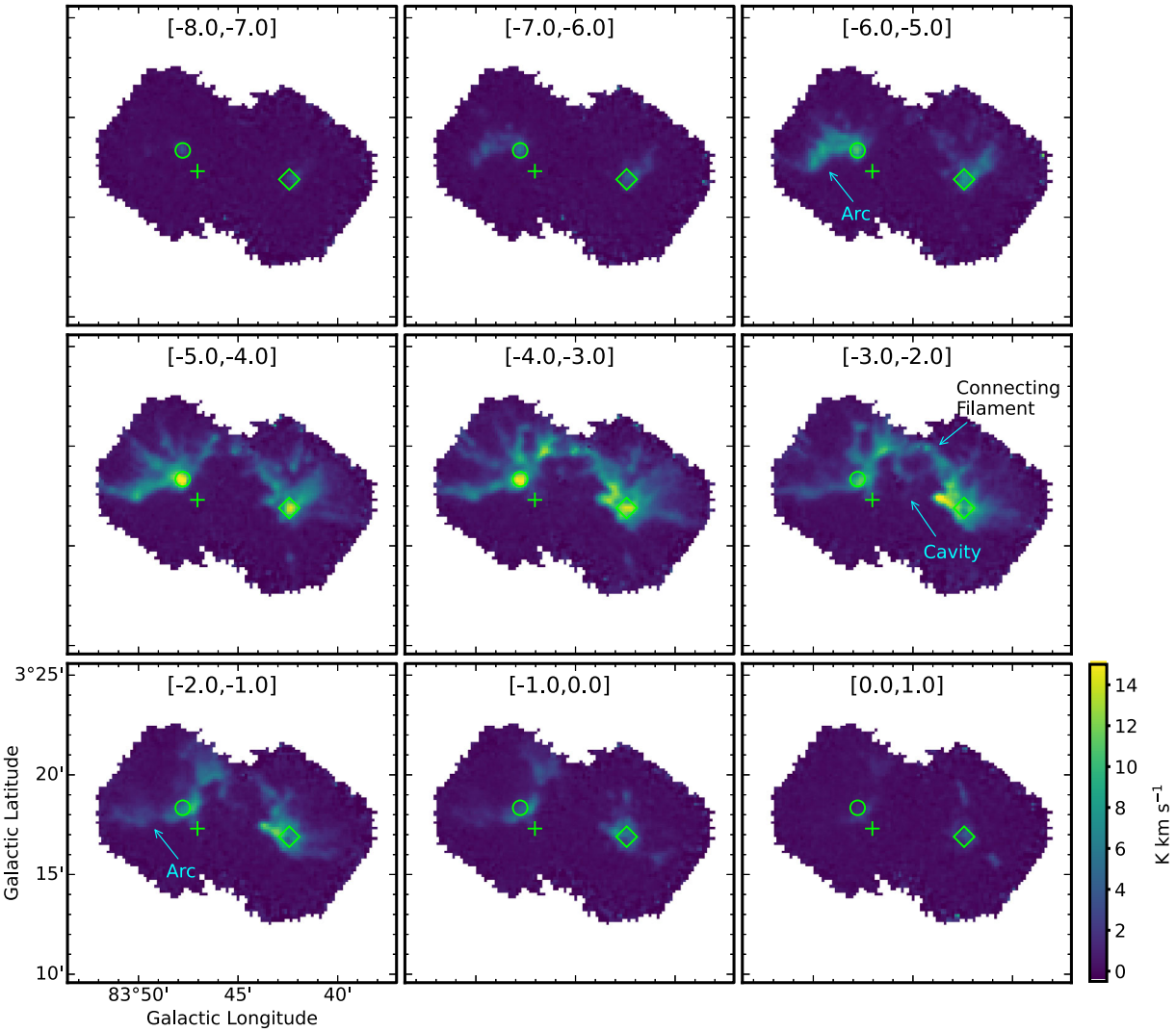

Figure 2. Channel maps of ^{13}CO(3-2) emission. Plus symbol marks the massive star BD+45 3216. Circle and diamond denote the locations of the two RMS sources, G083.7962+03.3058 and G083.7071+03.2817, respectively. An arc-like filamentary structure, a cavity-like structure and a connecting filament have been indicated by arrows.

CO(3-2) emission appears to be diffused with no particular discernible structure, which is expected, given the ubiquitous nature of CO molecule and comparatively lower critical density than the other two transitions. However, it is still worth noting that much of the CO (3-2) emission still 'faces away' from the massive star BD+45 3216. The ^{13}CO(3-2) m-0 map most clearly traces the molecular filamentary structures, which were examined in the channel maps (Figure 2). While the cavity to the west of the massive star shows no ^{13}CO(3-2) emission, the connecting filamentary structure between the eastern and western regions is prominent. Given that all emission here is at $\geq 5\sigma$ level, this indicates that there is significant molecular mass concentration in the connecting filament and it is not some minor emission structure. The critical density is highest for C^{18}O(3-2) transition, and thus, only the densest clumps are detected here. Unsurprisingly, the bulk of C^{18}O(3-2) emission is associated with the positions of RMS sources. The prominent arc-like filamentary structure marked on the ^{13}CO(3-2) channel map (Figure 2) is also partly seen in C^{18}O(3-2) m-0 map, indicating the presence of dense gas along it. The linewidth maps for all three transitions show a maxima toward the positions of the RMS sources as compared to the outer parts, which could be due to outflow activity and/or possibly suggest a convergence of different flows towards these sources. In the ^{13}CO(3-2) linewidth map, the connecting filament has a relatively lower velocity dispersion, while the arc-like filamentary structure (Figure 2) displays a relatively larger dispersion along its length as compared to others.

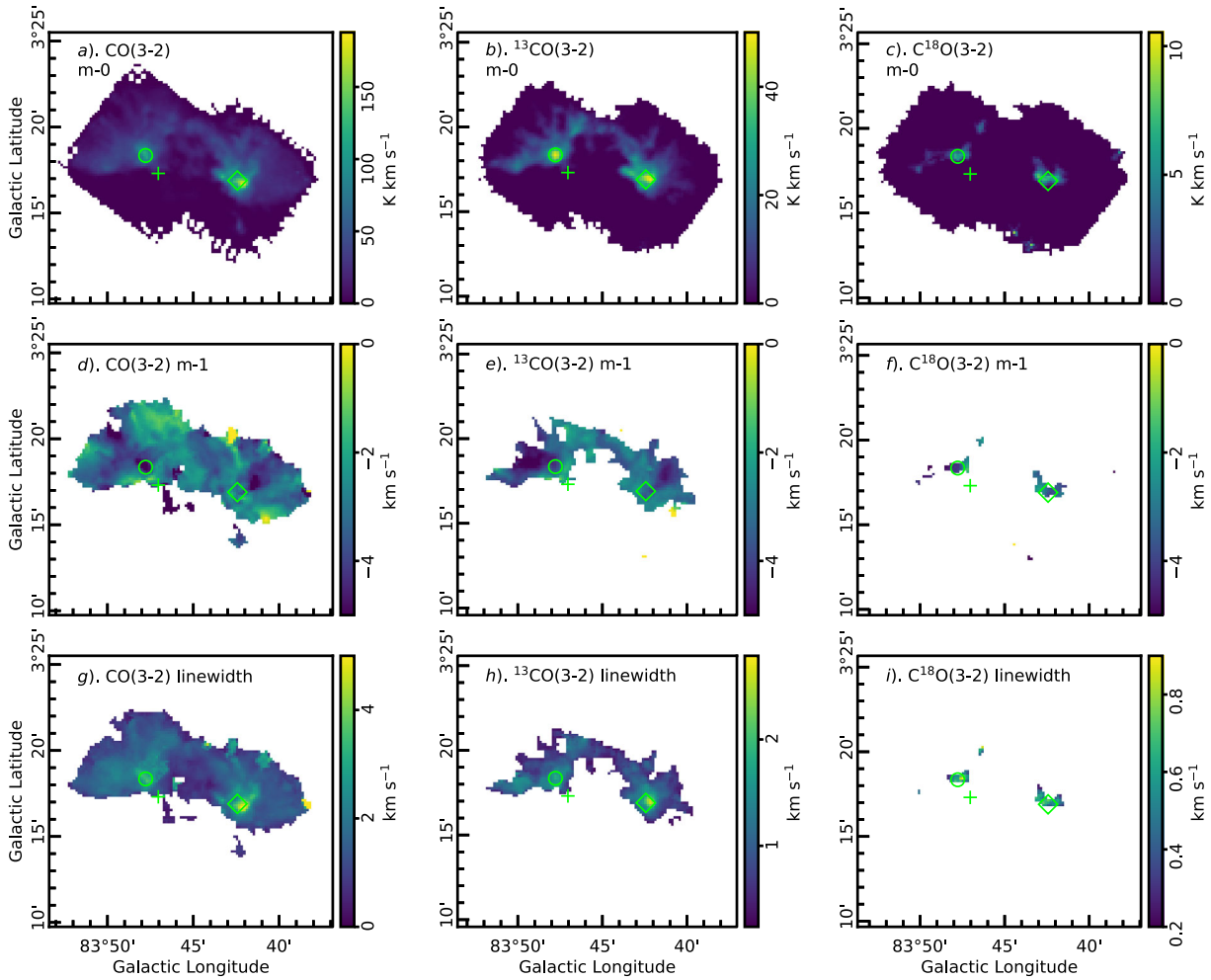

Figure 3. Row-wise: moment-0 (integrated intensity), moment-1 (intensity-weighed velocity) and linewidth (intensity-weighed dispersion) collapsed images for three cubes: CO(3-2), ^{13}CO(3-2), C^{18}O(3-2) in first, second and third columns, respectively. The symbols are same as Figure 2.

3.3 *Physical parameters*

Figure 4 shows the ^{13}CO(3-2) m-0 map of the region overlaid with the massive star BD+45 3216; the two RMS sources (G083.7962+03.3058 and G083.7071+03.2817); and the MSX sources (m1–m11), which lay in the regions of emission $\geq 5\sigma$ level (see Section 3.2). The local peaks of m-0 emission, based on visual examination of the contours have also been marked on the image (p1–p10). To obtain the physical parameters for these sources (except BD+45 3216, which did not have any molecular emission associated with it), we extracted the spectra at their locations (from a 2×2 pixel area). As high-velocity resolution is required for the calculations, the non-averaged cubes with the native channel width of $\sim$0.05 km s^{-1} were utilized for spectrum extraction.

For the RMS sources, both ^{13}CO(3-2) and C^{18}O(3-2) spectra were available, and are shown in Figure 5. However, for the MSX sources (m1–m11) and the local ^{13}CO(3-2) integrated emission peaks (p1–p10), only ^{13}CO(3-2) spectra could be extracted, shown in Figures 6 and 7, respectively. The results from the Gaussian fitting are given in Table 2. The first thing to notice is that at some of the locations, a simple Gaussian is a poor fit to the spectra. For example, in Figure 5, the spectra have broad wings on both sides, which is usually an indication of some kind of likely outflow associated with the sources. According to Maud *et al.* (2015b), while G083.7071+03.2817 is associated with an outflow, G083.7962+03.3058 has a possibility of the same. For some of the locations in Figures 6 and 7, there appears to be excess emission on the red side. It had been discussed in Section 3.1 that the arc-like structure in Figure 2 probably has a merger of blueshifted and redshifted filaments. The excess redshifted emission seen at the locations, which lie on this arc, i.e., m1

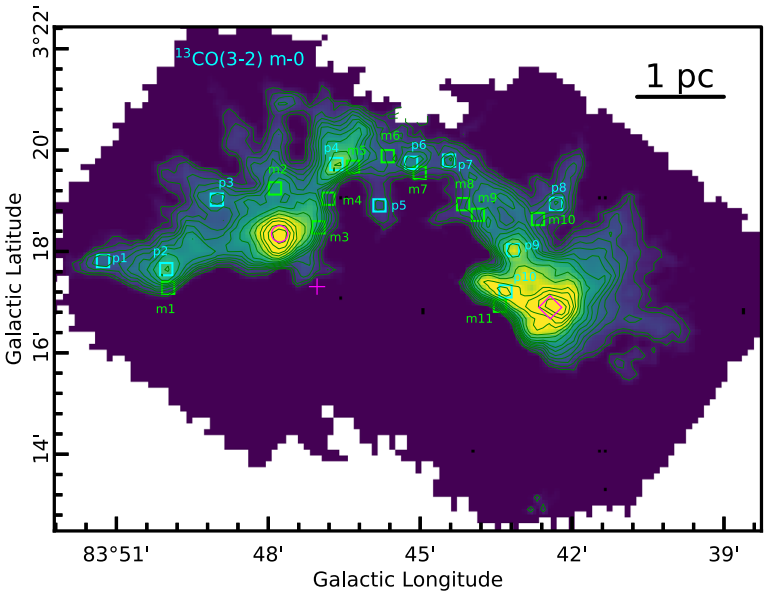

Figure 4. ^{13}CO(3-2) integrated intensity map (contours at 2, 3.5, 6, 8, 10, 12, 14, 17, 21, 25, 30, 34, 40 and 45 K km s^{-1}). Plus symbol marks the massive star BD+45 3216. The two RMS sources, G083.7962+03.3058 and G083.7071+03.2817, have been shown by circle and diamond symbols, respectively. The MSX sources have been marked in green boxes and labeled m1–m11. Cyan boxes (labeled p1–p10) are the locations of local contour peaks, where also we extracted the spectra.

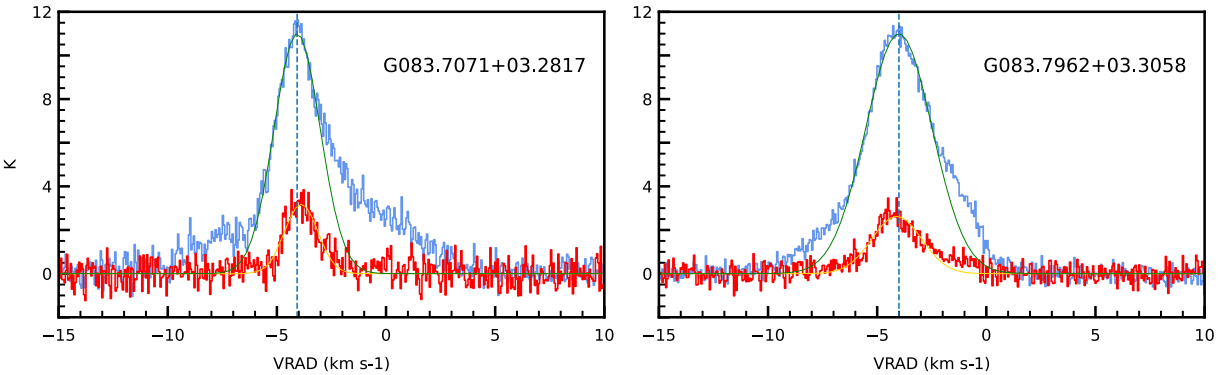

Figure 5. ^{13}CO(3-2) (blue) and C^{18}O(3-2) (red) spectra at positions of RMS sources marked in Figure 4. Green and yellow curves show the Gaussian fits to the respective spectra, with blue dashed line marking the velocity of the peak of ^{13}CO(3-2) Gaussian fit.

(Figure 6) and p1, p2 (Figure 7) could be an indication of the same. Emission peak positions, p8 and p9, display significant self-absorption in their spectra. The mean velocity for most of the fits lies in the range of −2.5 to −4.0 km s^{-1}. It is notable that the locations towards the eastern side (namely, p1, p2, p3 and m1) have significantly more blueshifted mean velocities as opposed to other locations. The RMS sources, though with wide wings, have nearly same mean velocities (∼−4.0 km s^{-1}), which is in agreement with the radial velocity for the Sh2-112 region in Blitz *et al.* (1982), Stark & Brand (1989) and Brand & Blitz (1993). Though our locations display a range of mean velocities, the overall distribution is consistent with other values cited in literature within error limits (Dobashi *et al.* 1994; Urquhart *et al.* 2008; Lumsden *et al.* 2013; Maud *et al.* 2015a, b; Panja *et al.* 2022).

Using the full width at half maxima (FWHM) returned by the fit, we calculate the standard deviation (or observed velocity dispersion), the non-thermal velocity dispersion and the total velocity dispersion using the following set of equations (Fuller & Myers 1992; Fiege & Pudritz 2000):

$$\Delta V_{\rm tot}^2 = \Delta V_{\rm obs}^2 + 8\ln 2\, kT \left(\frac{1}{\bar{m}} - \frac{1}{m_{\rm obs}}\right),$$

$$\Rightarrow \frac{\Delta V_{\rm tot}^2}{8\ln 2} = \frac{kT}{\bar{m}} + \left(\frac{\Delta V_{\rm obs}^2}{8\ln 2} - \frac{kT}{m_{\rm obs}}\right), \qquad (1)$$

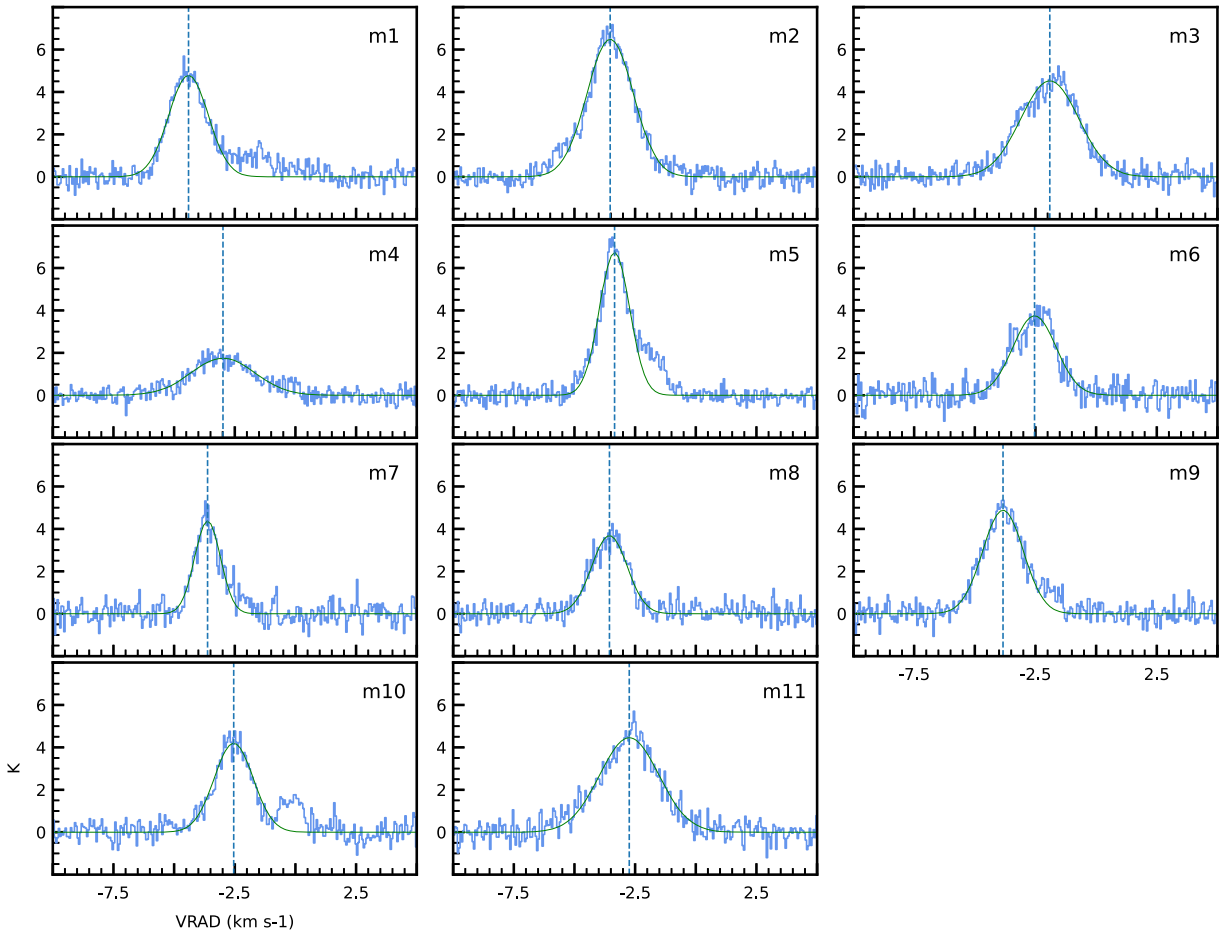

Figure 6. ^{13}CO(3-2) spectra at MSX source positions marked in Figure 4 (green boxes labeled m1–m11). Green curve depicts the Gaussian fit to the spectra, with blue dashed line marking the velocity of the peak of Gaussian fit.

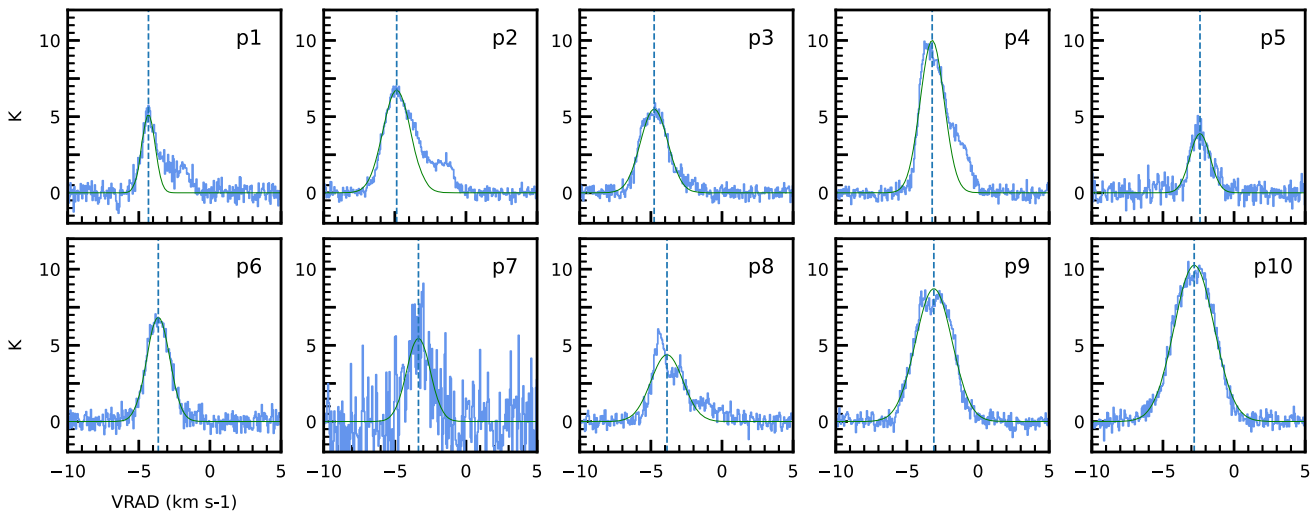

Figure 7. ^{13}CO(3-2) spectra at peak positions marked in Figure 4 (cyan boxes labeled p1–p10). Green curve depicts the Gaussian fit to the spectra, with blue dashed line marking the velocity of the peak of Gaussian fit.

Table 2. Parameters derived from ^{13}CO(3-2) spectra at the locations marked in Figure 4. For G083.7071+03.2817 and G083.7962+03.3058, C^{18}O(3-2) spectrum was also available and thus used for calculation as well.

Clump	Mean (km s^{-1})	FWHM (km s^{-1})	Amplitude (K)	σ_{NT} (km s^{-1})	Mach number	P_{TNT}	l (deg)	b (deg)
G083.7071+03.2817								
C^{18}O	−3.88	1.79	3.18	0.76	2.86	0.12	83.7071	03.2817
^{13}CO	−4.07	2.48	11.00	1.05	3.97	0.06	–	–
G083.7962+03.3058								
C^{18}O	−4.11	2.69	2.62	1.14	4.30	0.05	83.7962	3.3058
^{13}CO	−4.00	3.58	10.99	1.52	5.73	0.03	–	–
MSX sources								
m1	−4.41	1.92	4.78	0.81	3.06	0.11	83.8330	3.2881
m2	−3.53	2.24	6.48	0.95	3.59	0.08	83.7978	3.3207
m3	−1.91	2.81	4.52	1.19	4.49	0.05	83.7835	3.3079
m4	−2.99	3.09	1.75	1.31	4.95	0.04	83.7803	3.3174
m5	−3.35	1.47	6.74	0.62	2.34	0.18	83.7721	3.3279
m6	−2.54	2.09	3.75	0.89	3.34	0.09	83.7607	3.3313
m7	−3.62	1.25	4.38	0.53	1.99	0.25	83.7502	3.3258
m8	−3.56	1.72	3.68	0.73	2.74	0.13	83.7359	3.3156
m9	−3.84	1.97	4.88	0.83	3.15	0.10	83.7310	3.3121
m10	−2.54	1.89	4.20	0.80	3.02	0.11	83.7112	3.3107
m11	−2.74	2.87	4.45	1.22	4.60	0.05	83.7237	3.2822
m-0 contour peaks								
p1	−4.32	1.11	5.14	0.47	1.76	0.32	83.8544	3.2968
p2	−4.87	2.28	6.74	0.96	3.64	0.08	83.8336	3.2942
p3	−4.77	2.27	5.49	0.96	3.62	0.08	83.8170	3.3171
p4	−3.22	1.97	10.01	0.83	3.15	0.10	83.7776	3.3288
p5	−2.39	1.67	3.89	0.70	2.66	0.14	83.7634	3.3152
p6	−3.63	1.91	6.85	0.81	3.05	0.11	83.7530	3.3291
p7	−3.34	1.97	5.46	0.83	3.14	0.10	83.7405	3.3299
p8	−3.87	2.66	4.38	1.12	4.25	0.05	83.7053	3.3157
p9	−3.11	3.01	8.72	1.28	4.82	0.04	83.7194	3.3005
p10	−2.80	3.30	10.26	1.40	5.29	0.04	83.7219	3.2869

$$\Rightarrow \sigma_{tot}^2 = c_s^2 + (\sigma_{obs}^2 - \sigma_T^2), \quad (2)$$

$$= c_s^2 + \sigma_{NT}^2. \quad (3)$$

In the above equations, ΔV_{obs} is the FWHM of the fit; σ_{obs} ($=\Delta V_{obs}/\sqrt{8\ln 2}$ for Gaussian fits) is the standard deviation (or dispersion); σ_T ($=\sqrt{kT/m_{obs}}$) is the thermal velocity dispersion; m_{obs} is the mass of the relevant molecule (29 amu and 30 amu for ^{13}CO and C^{18}O, respectively); σ_{NT} is the non-thermal velocity dispersion; c_s ($=\sqrt{kT/\bar{m}}$) is the speed of sound; $\bar{m}$ is the average molecular weight of the medium (2.37 amu); and T is the excitation or gas kinetic temperature.

The FWHM shows a wide range at these locations, in the range of ∼1.5–3.0 km s^{-1} for most of the sources, with some of the highest values associated with locations in the vicinity of the two RMS sources, such as m2, m3, m4, m11 and p10. This tallies with the linewidth map in Figure 3(h). For the above calculations, we take the excitation temperature T as 20 K (see Figure 15 in Panja *et al.* 2022). Furthermore, we also calculate Mach number ($=\sigma_{NT}/c_s$) and the ratio of thermal to non-thermal pressure ($P_{TNT} = c_s^2/\sigma_{NT}^2$) (Lada *et al.* 2003) for each of the locations. The results of these two calculations show the presence of supersonic motion, and a dominance of non-thermal pressure in the cloud. The Mach number and P_{TNT} values are inversely correlated, as expected from their dependence on σ_{NT}. Such values would suggest that the emission mechanism is likely some supersonic non-thermal phenomena, and could be via turbulence and magnetic fields (Myers & Goodman 1988; Crutcher 1999), to suggest one such mechanism.

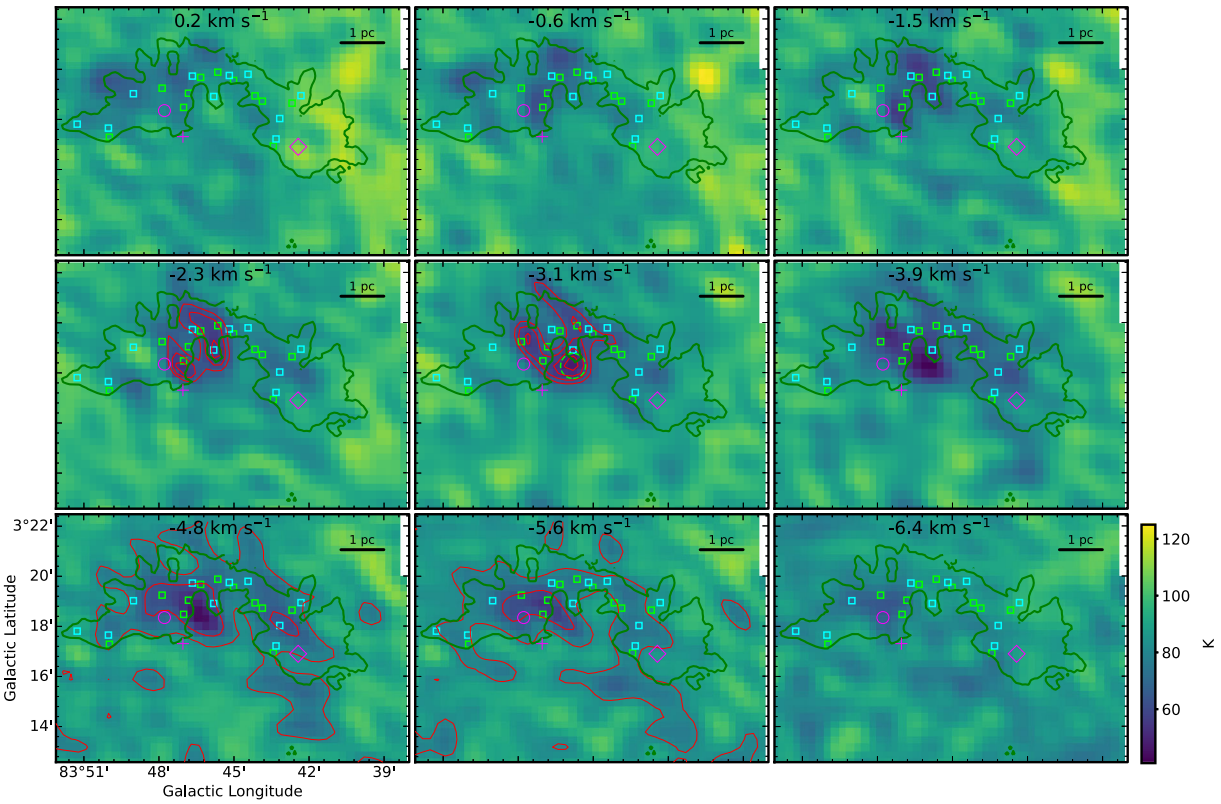

Figure 8. Velocity channel maps for the CGPS H I 21 cm emission. Green contour marks the 2 K km s^{-1} level of the ^{13}CO(3-2) m-0 (Figure 4) image. In −2.3 and −3.1 km s^{-1} channels, the red contours have been drawn at (outer to inner) 65, 60, 55 and 50 K; while in −4.8 and −5.6 km s^{-1} channels, the red contours are at 81 (outer) and 65 (inner) K. The dashed green circle in −3.1 km s^{-1} channel shows the location where spectrum was extracted (see Figure 9). The rest of the symbols are same as Figure 4.

4. Discussion

Figure 8 shows the CGPS 21 cm velocity channel maps of this region. The channel maps show a depression in H I emission (see Figure 9), which is (anti-)correlated with strong (i.e., $\geq 5\sigma$) molecular emission. Such features have been referred as H I self absorption (or HISA) features in literature, and have been found to be an extensive presence in 21 cm surveys (Kerton 2005; Wang *et al.* 2020). HISA regions indicate the presence of cold H I gas in foreground against warm H I emission from background. In our channel maps, most intense depression in emission seems to be confined to the north-eastern quadrant, in the vicinity of the source G083.7962+03.3058 (circle). Channels −2.3 km s^{-1} and −3.1 km s^{-1} display shell-like feature on a smaller spatial scale, while the channels −4.8 km s^{-1} and −5.6 km s^{-1} show large scale shell-like feature. The anti-correlation of molecular emission and depression in H I emission can be most prominently seen in the −4.8 km s^{-1} and −5.6 km s^{-1} channels. Such shell-like features have been found in other regions as well, such as Sh2-237 (Dewangan *et al.* 2017), W4 and W5 (Hosokawa & Inutsuka 2007) and in Southern Galactic Plane Survey (SGPS) regions (McClure-Griffiths *et al.* 2001).

Figure 10 shows the ^{13}CO(3-2) m-0 image (overlaid with NVSS contours), the Hα image of the region and the continuum-subtracted H_2 emission map of the region from Panwar *et al.* (2020). The radio emission seems to have multiple peaks, and on a comparison of Figures 4 and 10(a), the radio peaks appear to be associated with the locations of m3/m4, p5 and a location to the east of p10. According to Panwar *et al.* (2020), the location to the east of p10 is the ionized boundary layer. Based on the presence of this ionized boundary layer and pressure calculations, they further conjecture the possibility of triggered star formation towards the location of RMS source G083.7071+03.2817 due to O8V type star BD+45 3216 (also see Morgan *et al.* 2004, 2009; Urquhart *et al.* 2009). It is possible that the expansion of the ionized gas could have had a role in the formation of the cavity towards the west/northwest of the massive star BD+45 3216. There is significant Hα emission in the cavity, while the H_2 2.12 μm emission seems to trace the southern boundary of the molecular cloud. All along the cavity perimeter, there

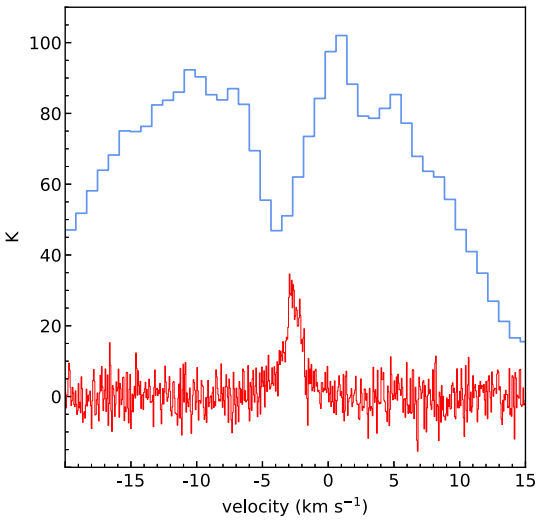

Figure 9. ^{13}CO(3-2) spectrum (in red) and CGPS H I spectrum (in blue) at the location marked in Figure 8 (green circle in −3.1 km s^{-1} channel)—demonstrating the H I self-absorption feature centered at ∼[−5, −4] km s^{-1} and its anti-correlation with the molecular emission. The ^{13}CO(3-2) spectrum has been scaled up by a factor of 30× for better visibility.

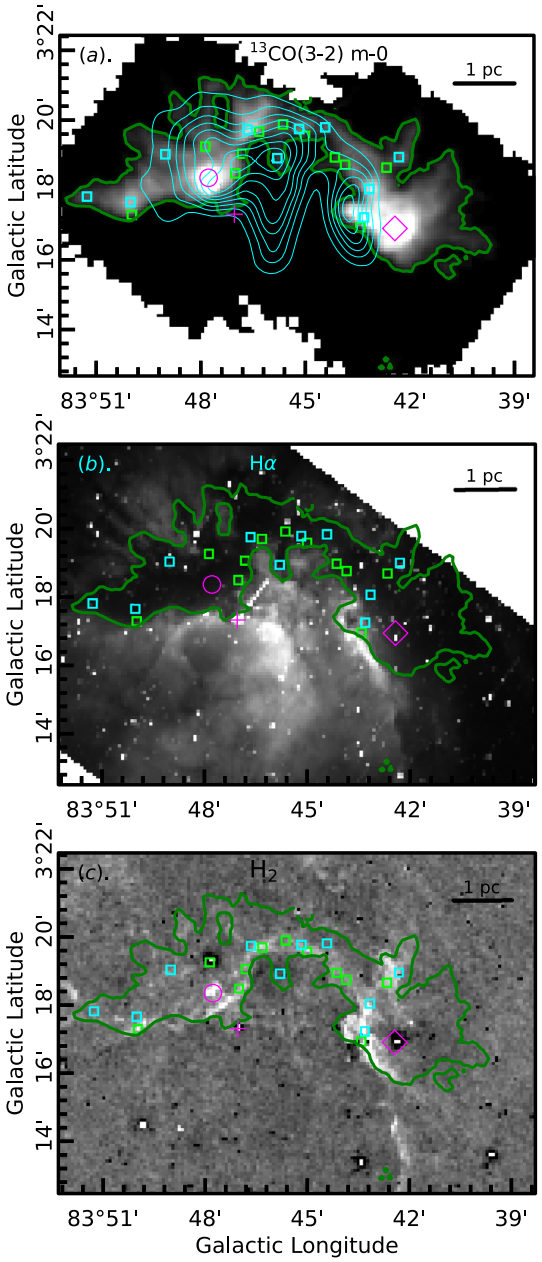

Figure 10. (a) ^{13}CO(3-2) m-0 map. Cyan contours are NVSS levels at 0.01, 0.02, 0.03, 0.04, 0.05, 0.06, 0.07, 0.08, 0.09 and 0.1 Jy beam^{-1}. (b) Hα image of the region. (c) Continuum-subtracted H_2 emission (2.12 μm) map from Panwar *et al.* (2020). Green contour marks the 2 K km s^{-1} level of the ^{13}CO(3-2) m-0 (Figure 4) image. The rest of the symbols are same as Figure 4.

are finger-like filamentary structures protruding into it, reminiscent of bright-rimmed clouds which are seen in optical and infrared emissions (Chauhan *et al.* 2011; Sharma *et al.* 2016). Here, these structures are seen in absorption in optical (Figure 10b) and in emission in ^{13}CO(3-2) integrated intensity map (Figure 10a). Two out of three of these finger-like structures seem to be hosting molecular peaks at their ends, i.e., p5 and p10. If there is a possible case of triggering towards the source G083.7071+03.2817, then, based on size considerations of the cavity, there could be possible triggering all along the cavity perimeter. The MSX sources m3, m4, m5, m7, m8, m9 and m11 seem to be distributed along the cavity boundary, where there is seemingly compression of molecular material, as evidenced by the sharp change in ^{13}CO(3-2) contour levels (see Figure 4).

Lastly, we present the position–velocity maps in Figure 11 along the different line segments marked L1–L8 on the central image. While the lines L1–L5 trace the filamentary structures, which converge on the source G083.7962+03.3058 (circle), L6–L8 are cuts along the filamentary structures associated with G083.7071+03.2817 (diamond symbol). The position–velocity maps show a complex structure with clumping along their length. Significant velocity gradients can also be seen in most of them, and especially in L1–L5 in the vicinity of the source G083.7962+03.3058 (i.e., bright clump towards the right in L1–L5). Here, we note that such a gradient could indicate gas being channeled toward the source, and such a flow of gas along the filamentary structures towards the RMS sources—G083.7962+03.3058 and G083.7071+03.2817—as also discussed in Section 3.2, is similar to the longitudinal flow in filaments towards hubs in hub-filament systems (Dewangan *et al.* 2017, 2020; Williams *et al.*

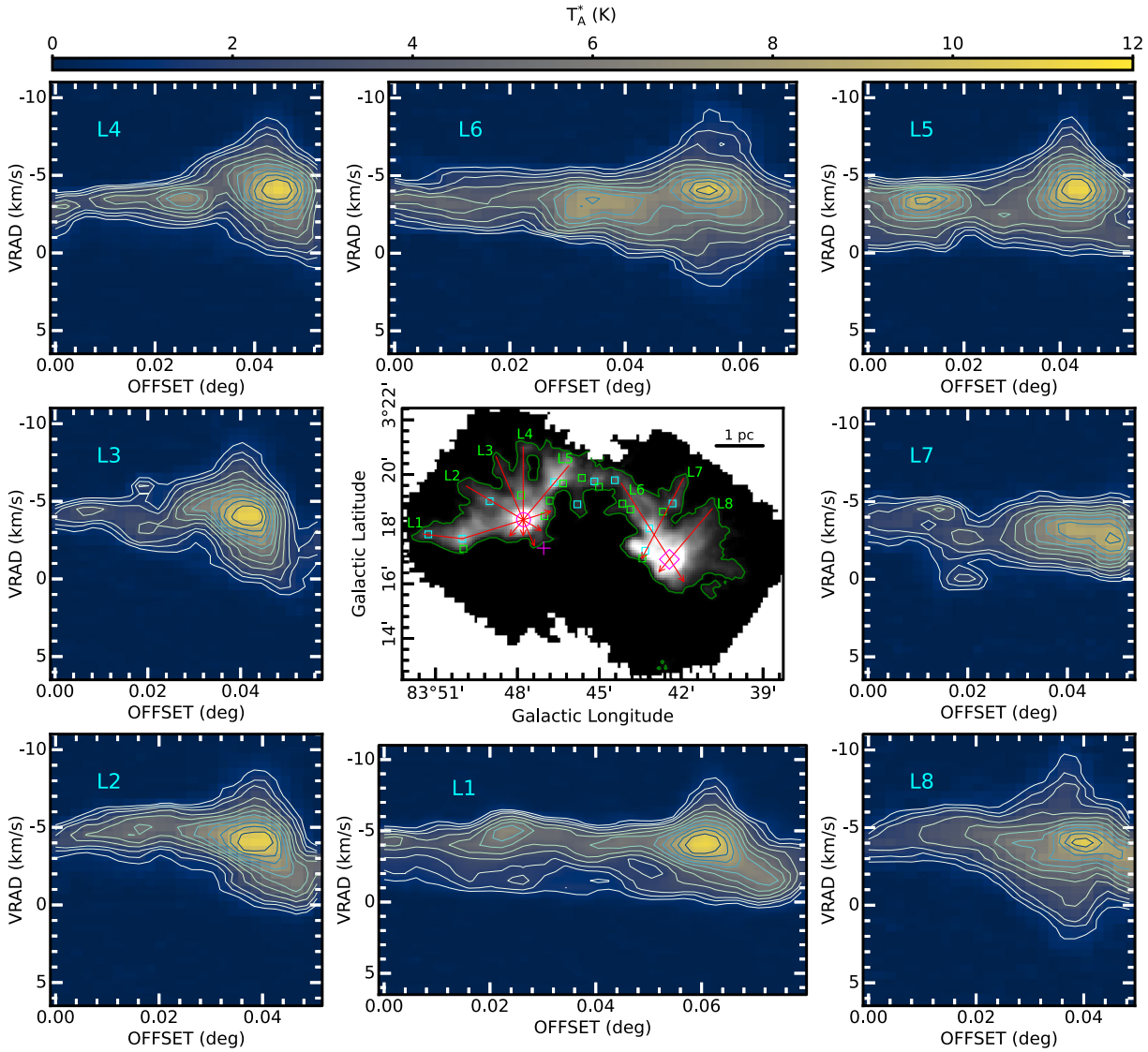

Figure 11. Position–velocity diagrams for the line segments marked L1–L8 (in red) on the central image (^{13}CO(3-2) m-0 from Figure 4). Green contour marks the 2 K km s^{-1} level of the ^{13}CO(3-2) m-0 (Figure 4) image. The rest of the symbols are same as Figure 4. On the L1–L8 p–v maps, the contour levels are at 1, 1.5, 2, 3, 4, 5, 6, 7, 8, 9 and 10 K.

2018). Therefore, this region could present a good example of exploring various star formation frameworks, such as global hierarchical collapse (GHC; Vázquez-Semadeni *et al.* 2019), conveyor belt model (Longmore *et al.* 2014; Krumholz & McKee 2020), filaments to clusters model (Kumar *et al.* 2020), to name a few.

According to Panja *et al.* (2022), the column density of the molecular emission region has been calculated as $\sim 10^{22}$ cm^{-2}. Such regions have been designated as 'hubs' in the context of hub-filament systems in literature (Myers 2009). The column density maps by Panja *et al.* (2022) also suggest such a hub-filament configuration for the larger region of the order of a few tens of parsec encompassing Sh2-112. Thus, what we have explored here seems to be the detailed structure of a hub region, where massive star formation is going on. However, given the importance of filamentary structures in star formation and expositions of various filament types in literature (see Hacar *et al.* 2022, for a detailed review), it is essential to further study such regions via high spectral and spatial resolution molecular transitions of other species, magnetic fields, and so on, so as to understand the evolution of molecular clouds as they form stars.

5. Summary and conclusions

We have carried out an analysis of the Sh2-112 region in CO(3-2), ^{13}CO(3-2) and C^{18}O(3-2) molecular line

transitions from the JCMT, supported by archival data from CGPS H I line, MSX, NVSS and IPHAS Hα for visual examination. Our main conclusions are as follows:

1. The molecular emission appears filamentary in channel maps and seems to be directed away from the massive star BD+45 3216, which is also located at the edge of a cavity-like structure.
2. Multiple local peaks were found associated with the molecular emission in the ^{13}CO(3-2) integrated intensity emission map (m-0) which was generated using clumps detected above 5σ level in the position–position–velocity space. The linewidth map shows high dispersion associated with the positions of the RMS sources (G083.7962+03.3058 and G083.7071+03.2817).
3. Analysis of CGPS 21 cm H I line emission reveals the presence of shell-like HISA feature, where the molecular emission is nearly coincident with the depression in H I emission.
4. ^{13}CO(3-2) spectra was extracted at the locations of RMS sources, MSX sources and the local peaks of emission. For the RMS sources, C^{18}O(3-2) spectra was also extracted. Spectral profile fitting suggests significant deviation from a Gaussian profile for many sources. All the locations were found to have significant non-thermal dispersions; large Mach numbers (∼2–6) indicating dominance of supersonic motions within the clumps; and a small thermal to non-thermal pressure ratio (∼0.03–0.3).

Acknowledgements

We thank the anonymous referee for a critical reading of the manuscript and for the suggestions in the improvement of this paper. DKO acknowledges the support of the Department of Atomic Energy, Government of India, under project Identification No. RTI 4002. The James Clerk Maxwell Telescope has historically been operated by the Joint Astronomy Centre on behalf of the Science and Technology Facilities Council of the United Kingdom, the National Research Council of Canada and the Netherlands Organization for Scientific Research. This research has made use of the NASA/IPAC Infrared Science Archive, which is funded by the National Aeronautics and Space Administration and operated by the California Institute of Technology. This research made use of data products from the Midcourse Space Experiment. Processing of the data was funded by the Ballistic Missile Defense Organization with additional support from NASA Office of Space Science. This research has also made use of the NASA/IPAC Infrared Science Archive, which is operated by the Jet Propulsion Laboratory, California Institute of Technology, under contract with the National Aeronautics and Space Administration. This research has made use of the services of the ESO Science Archive Facility.

References

Barentsen G., Farnhill H. J., Drew J. E., *et al.* 2014, MNRAS, 444, 3230. https://doi.org/10.1093/mnras/stu1651
Berry D. S., Reinhold K., Jenness T., *et al.* 2007, Astron. Data Anal. Softw. Syst. XVI, 376, 425
Blitz L., Fich M., Stark A. A. 1982, ApJS, 49, 183. https://doi.org/10.1086/190795
Brand J., Blitz L. 1993, A&A, 275, 67
Buckle J. V., Hills R. E., Smith H., *et al.* 2009, MNRAS, 399, 1026. https://doi.org/10.1111/j.1365-2966.2009.15347.x
Buckle J. V., Curtis E. I., Roberts J. F., *et al.* 2010, MNRAS, 401, 204. https://doi.org/10.1111/j.1365-2966.2009.15619.x
Burov A. B., Vdovin F. V., Zinchenko I. I., *et al.* 1988, Pisma v Astronomicheskii Zhurnal, 14, 492
Chauhan N., Pandey A. K., Ogura K., *et al.* 2011, MNRAS, 415, 1202. https://doi.org/10.1111/j.1365-2966.2011.18742.x
Condon J. J., Cotton W. D., Greisen E. W., *et al.* 1998, AJ, 115, 1693. https://doi.org/10.1086/300337
Crutcher R. M. 1999, ApJ, 520, 706. https://doi.org/10.1086/307483
Currie M. J., Berry D. S., Jenness T., *et al.* 2014, Astron. Data Anal. Softw. Syst. XXIII, 485, 391
Dewangan L. K., Ojha D. K., Zinchenko I., *et al.* 2017, ApJ, 834, 22. https://doi.org/10.3847/1538-4357/834/1/22
Dewangan L. K., Ojha D. K., Sharma S., *et al.* 2020, ApJ, 903, 13. https://doi.org/10.3847/1538-4357/abb827
Dickel H. R., Wendker H., Bieritz J. H. 1969, A&A, 1, 270
Dobashi K., Bernard J.-P., Yonekura Y., *et al.* 1994, ApJS, 95, 419. https://doi.org/10.1086/192106
Dobashi, K., Bernard J.-P., Fukui Y. 1996, ApJ, 466, 282. https://doi.org/10.1086/177509
Drew J. E., Greimel R., Irwin M. J., *et al.* 2005, MNRAS, 362, 753. https://doi.org/10.1111/j.1365-2966.2005.09330.x
Egan M. P., Price S. D., Kraemer K. E. 2003, AAS
Elmegreen B. G. 1998, Origins, 148, 150
Elmegreen B. G. 2011, EAS Publ. Ser., 51, 45. https://doi.org/10.1051/eas/1151004
Fiege J. D., Pudritz R. E. 2000, MNRAS, 311, 85. https://doi.org/10.1046/j.1365-8711.2000.03066.x
Fuller G. A., Myers P. C. 1992, ApJ, 384, 523. https://doi.org/10.1086/170894

Hacar A., Clark S., Heitsch F., *et al.* 2022, arXiv:2203.09562
Hoare M. G., Lumsden S. L., Oudmaijer R. D., *et al.* 2005, Massive Star Birth: A Crossroads of Astrophysics, 227, 370. https://doi.org/10.1017/S174392130500476X
Hosokawa T., Inutsuka S. 2007, ApJ, 664, 363. https://doi.org/10.1086/518396
Israel F. P. 1978, A&A, 70, 769
Kerton C. R. 2005, ApJ, 623, 235. https://doi.org/10.1086/428490
Kumar M. S. N., Palmeirim P., Arzoumanian D., *et al.* 2020, A&A, 642, A87. https://doi.org/10.1051/0004-6361/202038232
Krumholz M. R., McKee C. F. 2020, MNRAS, 494, 624. https://doi.org/10.1093/mnras/staa659
Lada C. J., Bergin E. A., Alves J. F., *et al.* 2003, ApJ, 586, 286. https://doi.org/10.1086/367610
Lahulla J. F. 1985, A&AS, 61, 537
Longmore S. N., Kruijssen J. M. D., Bastian N., *et al.* 2014, Protostars and Planets VI, 291. https://doi.org/10.2458/azu_uapress_9780816531240-ch013
Lumsden S. L., Hoare M. G., Oudmaijer R. D., *et al.* 2002, MNRAS, 336, 621. https://doi.org/10.1046/j.1365-8711.2002.05785.x
Lumsden S. L., Hoare M. G., Urquhart J. S., *et al.* 2013, ApJS, 208, 11. https://doi.org/10.1088/0067-0049/208/1/11
Maud L. T., Lumsden S. L., Moore T. J. T., *et al.* 2015a, MNRAS, 452, 637. https://doi.org/10.1093/mnras/stv1334
Maud L. T., Moore T. J. T., Lumsden S. L., *et al.* 2015b, MNRAS, 453, 645. https://doi.org/10.1093/mnras/stv1635
McClure-Griffiths N. M., Dickey J. M., Gaensler B. M., *et al.* 2001, PASA, 18, 84. https://doi.org/10.1071/AS01010
Morgan L. K., Thompson M. A., Urquhart J. S., *et al.* 2004, A&A, 426, 535. https://doi.org/10.1051/0004-6361:20040226
Morgan L. K., Urquhart J. S., Thompson M. A. 2009, MNRAS, 400, 1726. https://doi.org/10.1111/j.1365-2966.2009.15585.x
Motte F., Bontemps S., Louvet F. 2018, ARA&A, 56, 41. https://doi.org/10.1146/annurev-astro-091916-055235
Myers P. C., Goodman A. A. 1988, ApJ, 329, 392. https://doi.org/10.1086/166385
Myers P. C. 2009, ApJ, 700, 1609. https://doi.org/10.1088/0004-637X/700/2/1609
Ogura K. 2010, ASI Conf. Ser., 1, 19
Panja A., Sun Y., Chen W. P., *et al.* 2022, ApJ, 939, 46. https://doi.org/10.3847/1538-4357/ac940f
Panwar N., Sharma S., Ojha D. K., *et al.* 2020, ApJ, 905, 61. https://doi.org/10.3847/1538-4357/abc42e
Price S. D., Egan M. P., Carey S. J., *et al.* 2001, AJ, 121, 2819. https://doi.org/10.1086/320404
Sharma S., Pandey A. K., Borissova J., *et al.* 2016, AJ, 151, 126. https://doi.org/10.3847/0004-6256/151/5/126
Sharpless S. 1959, ApJS, 4, 257. https://doi.org/10.1086/190049
Stark A. A., Brand J. 1989, ApJ, 339, 763. https://doi.org/10.1086/167334
Taylor A. R., Gibson S. J., Peracaula M., *et al.* 2003, AJ, 125, 3145. https://doi.org/10.1086/375301
Urquhart J. S., Busfield A. L., Hoare M. G., *et al.* 2008, A&A, 487, 253. https://doi.org/10.1051/0004-6361:200809415
Urquhart J. S., Morgan L. K., Thompson M. A. 2009, A&A, 497, 789. https://doi.org/10.1051/0004-6361/200811149
Uyanıker B., Fürst E., Reich W., *et al.* 2001, A&A, 371, 675. https://doi.org/10.1051/0004-6361:20010387
Vázquez-Semadeni E., Palau A., Ballesteros-Paredes J., *et al.* 2019, MNRAS, 490, 3061. https://doi.org/10.1093/mnras/stz2736
Wang Y., Bihr S., Beuther H., *et al.* 2020, A&A, 634, A139. https://doi.org/10.1051/0004-6361/201935866
Williams J. P., de Geus E. J., Blitz L. 1994, ApJ, 428, 693. https://doi.org/10.1086/174279
Williams G. M., Peretto N., Avison A., *et al.* 2018, A&A, 613, A11. https://doi.org/10.1051/0004-6361/201731587
Zinnecker H., Yorke H. W. 2007, ARA&A, 45, 481. https://doi.org/10.1146/annurev.astro.44.051905.092549